SS-BSAR WITH GNSS AND A STATIONARY RECEIVER — EXPERIMENTAL RESULTS

Zhangfan Zeng[*]

Microwave Integrated System Lab, University of Birmingham, B15 2TT, UK

Abstract—This paper presents experimental results in the study of Space-surface Bistatic SAR (SS-BSAR) with global navigation satellite system (GNSS) and stationary receiver. The system uses GNSS as the transmitter of opportunity and a self-built, low cost receiver being set-up and fixed on the earth. It is potentially useful at remote sensing applications such as earth monitoring. The system prototype and signal processing at each stage leading to final image are described. Experimental image analysis is the core of this paper, and therefore performed in details finally.

1. INTRODUCTION

SS-BSAR is a novel and active involvement in bistatic SAR community in past decade [1–5]. It consists of a spaceborne transmitter and a receiver located on or near the earth. The transmitter can be any satellite, either cooperative radar satellite, or non-cooperative communication/navigation satellite. While the receiver could be either moving on the vehicle, or fixed on the ground.

In the current research, we only consider SS-BSAR with GNSS as the transmitter of opportunity and a stationary receiver (Figure 1). This configuration will be developed for deformation monitoring as its final use [5]. There are four global navigation satellite systems proposed all over the world, they are GPS from US, GLONASS from Russian, Galileo from EU and Beidou from China. Among the four, GPS cannot provide enough resolution (100 m), Galileo and Beidou are at its infancy and not reliable. GLONASS is the only choice regarding radar performance and system reliability. Though the choice of GNSS is outmatched by imaging satellite in terms of power budget

and resolution, these parameters would be adequate at long observation time. Moreover, it can provide following advantages: first, it ensures the all-day, all-weather monitoring, due to that large constellation of satellites (at least 4) could always be seen in the sky. Second, it can provide reliable operation, since global navigation satellite systems rarely fail, if any, the information could be checked on formal webpage beforehand. Third, GLONASS benefits at much lower revisit time (8 days) than Envisat satellite (35 days [6]). Furthermore, given large satellites on the sky, an optimal angle of observation and spatial resolution could be achieved by selecting proper satellite.

University of Birmingham (UOB) is the pioneer in the search of SS-BSAR from beginning, both on theoretical and experimental level. Through their work, the transmitter is GLONASS, while the receiver is mounted on the slow moving car with speed around 20 km/h. The radar performance such as power budget and resolution analysis could be found in [7, 8]. The signal synchronization and associated performance analysis could be found in [9]. The bistatic image formation algorithm could be referring to [10, 11]. Regarding stationary receiver case, a brief letter has reported to prove the system feasibility, however, no detailed image analysis was ever given [12].

The colleagues in UPC are also advanced in the investigation of such an asymmetric system, aimed at getting high quality image and interferometry products. Unlike UOB, they use imaging satellite as the transmitter source such as ENVISAT and TerraSAR-X. They developed their own experimental prototype and signal processing software [13, 14]. The promising results verified their system feasibility and showed potential diverse applications from such a system.

This article stresses on the imaging issue with proposed configuration from experimental point of view. In order to achieve the target, we should be aware of following challenges: the first is the signal synchronization between transmitter and receiver. In monostatic or cooperative bistatic radar system, the oscillator is either commonly in-use or known each other. In uncooperative system like us, however, this convenience no longer exists. The serious impacts resulted from failure of synchronization would cause image quality degradation (defocusing, unequal in sidelobes, etc.) [15]. Furthermore, the asymmetric topology inherent in SS-BSAR makes imaging more complex. The Bistatic topology has been classified in [16] in terms of complexity and SS-BSAR is indicated the most advanced one — general configuration. In this configuration, echo characteristic changes for different targets in both range and azimuth directions, resulting in inhomogeneous reference signals for each range and azimuth bin.

Apart from difficulty inherent in SS-BSAR mentioned above, it

could be found a more challenge task in stationary receiver by involving long dwelling time, in the order of 5 minutes, aimed at approaching satisfying resolution and signal-to-noise ratio. On one hand, with the dwelling time increasing, the discrepancy between real satellite ephemeris and nominal satellite positions accelerates, resulting in accumulating phase history offset. On the other hand, the data size will become considerate in our system. As such, a more robust and efficient synchronization algorithm other than one in [9] would be re-engineered.

This paper presents SS-BSAR imaging procedure from all aspects. The finally obtained experimental images prove that the system can provides stable and exciting performance. Section 2 describes the experimental prototype used to collect raw data. Section 3 briefly mentions the novel signal synchronization method and estimated parameters, with comparison to old one. Section 4 goes through the image formation algorithm leading to the bistatic experimental image. Section 5 is the core of this paper, it reports latest imagery results of two experiments, with a detailed analysis associated. Finally we conclude our work and propose future research directions.

2. EXPERIMENT PROTOTYPE

The experimental prototype comprises a two-channel super-heterodyne receiver. The receiver architecture is shown in Figure 2(a). After signal being received, it will pass through 3-stage down-converter (radio frequency stage, intermediate frequency stage and baseband stage). The baseband signal is then going through a quadrature demodulator, where it will be split into I and Q channel. Finally they are digitised
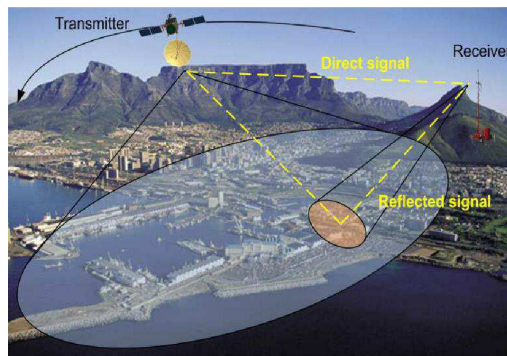

Figure 1. Illustration of SS-BSAR with GNSS and a stationary receiver.
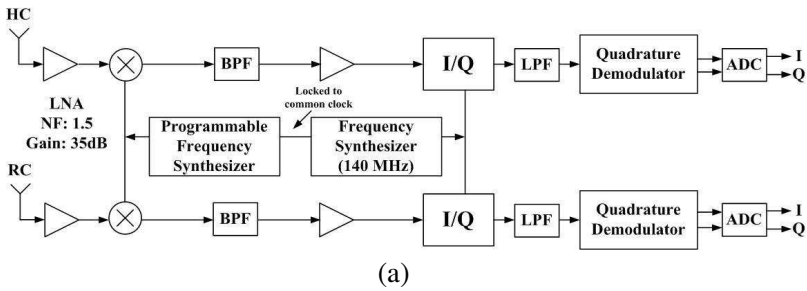
(a)

(b)

(c)

(d)

Figure 2. (a) Block diagram of receiver, (b) photograph of receiver box, (c) HC antenna, (d) RC antenna.

and stored to a PC with a sampling frequency of 50 MHz.

The receiver consists of two identical receiving channels. The first channel is called the heterodyne channel (HC). It utilises a wide beam antenna (Figure 2(c)) to receive the direct signal from the satellite. The omni-directional antenna ensures that the satellite is within its field of view for the whole dwell time. The other channel, called the radar channel (RC), uses a directional antenna (Figure 2(d)) to receive satellite signal reflections from an area of interest.

As Figure 2(a) indicates, both channels share the same clocks and frequency mixers, so clock slippage effects and local oscillator drift are common. However, the signal-to-noise ratio (SNR) of the direct signal is significantly higher, and therefore the signal in the HC is used for synchronisation.

3. SYNCHRONIZATION

The main role for synchronization is to align the time, frequency and phase information between transmitter and receiver, leading to
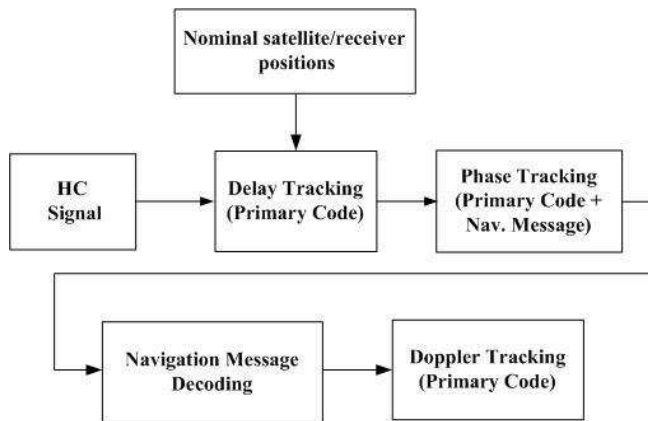
Figure 3. Block diagram of synchronization algorithm.

coherent signal processing. A novel synchronization algorithm has been developed to solve the large data size problem embedded in stationary receiver SS-BSAR. The use of this algorithm narrows the processing time (data size: 8 Gbyte) to 12 hours rather than 1 week by old synchronization algorithm reported in [9]. The block diagram of proposed algorithm is shown in Figure 3.

First, the HC signal is correlated with locally generated reference signal under the help of instantaneous nominal satellite and HC receiver position to find out the delay information of primary code (P-code in our case) in every pulse repetition interval (PRI). Next, the phase information of the peak position signal will be extracted, that includes primary code and navigation message. The navigation message is then decoded, leaving only primary code for processing. Finally the Doppler information of primary code is tracked by phase variation rate of navigation-free signal.

It is useful to compare the performance of new synchronization algorithm with old one, which has already been proved adequately functional [9]. Figure 4 shows the synchronization results including delay, Doppler and phase spectrum, obtained from two synchronization algorithms respectively. The data was arbitrarily taken from one of our real experiments.

It could be obviously found that, from new algorithm, the curve of delay is smooth, without any spikes; the azimuth frequency spectrum is flat, implying azimuth signal chirp like. Furthermore, the results from two algorithms are much the same, without visible discrepancies. It is also the reason why they were put in different plots, not superimposed together. In this way, we verified our new

synchronization algorithm, particular for accommodating stationary receiver SS-BSAR. The efficiency increases by more than 3 times. Due to that the emphasis of this paper is experimental imagery analysis, the detailed description of this synchronization method is omitted here, while it is in progress for another paper.

4. IMAGE FORMATION

The next step after synchronization is image inversion. The image formation algorithm utilized for our configuration is based on generic bistatic back-projection algorithm (BPA). Comparing to frequency domain algorithm limitation, such a choice is rationale. First, it is immune to any geometry limitation (there is no mature frequency domain eligible to general configuration); second, assumption of straight transmitter trajectory is not necessary for BPA (several minutes' satellite moving path will not be a straight line, and the DFT operation used in frequency domain algorithm cannot be used under this scenario). A block diagram of this modified algorithm is shown in Figure 5.
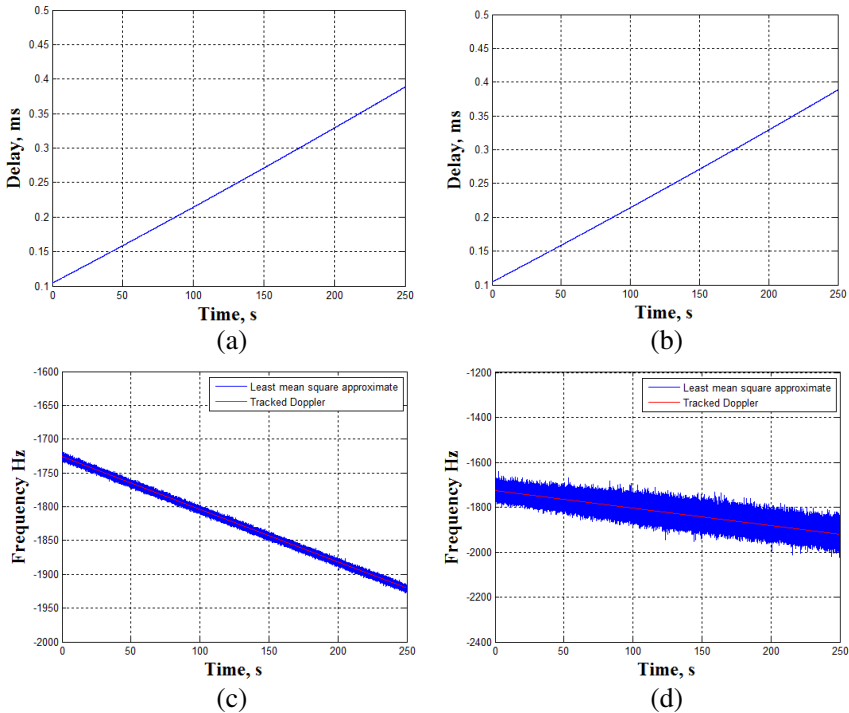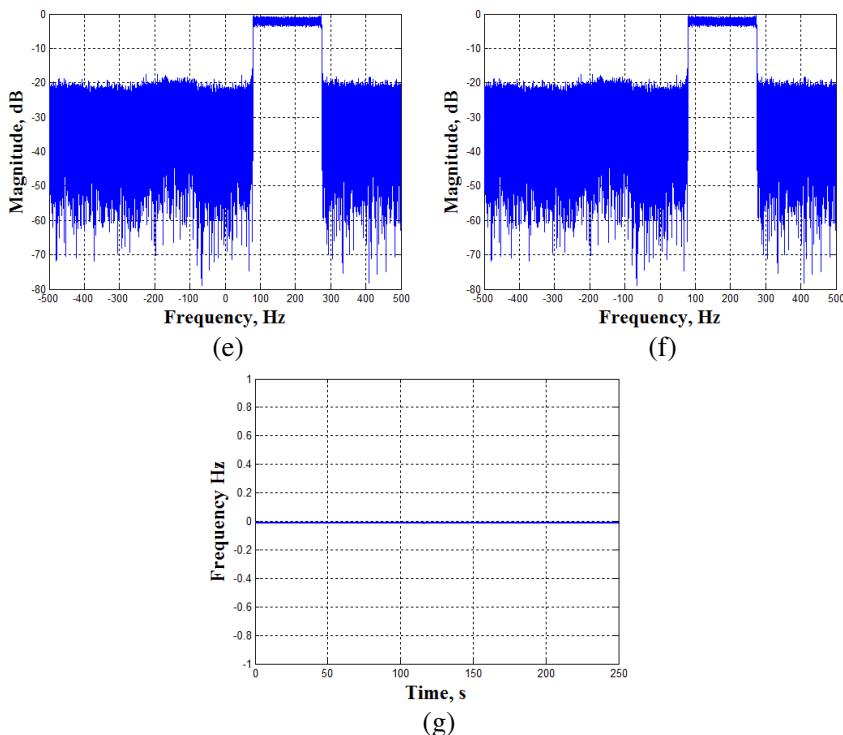
Figure 4. Synchronization results: (a) tracked delay using old algorithm, (b) tracked delay using new algorithm, (c) tracked Doppler using old algorithm, (d) tracked Doppler using new algorithm, (e) tracked slow-time phase spectrum after navigation message removal using old algorithm, (f) tracked slow-time phase spectrum after navigation message removal using new algorithm, (g) difference of Doppler frequency tracked from old and new algorithm.

Due to that BPA is well known and commonly used in research community and industry, more words are put here to show how the synchronization parameters are integrated in BPA before arriving at final image.

Following synchronization, we get the tracked delay, Doppler and phase information. Meanwhile, the nominal three parameters could be obtained by instantaneous satellite positions and receiver positions. The differences between these two are called residual delay, Doppler and phase, which include the errors such as local oscillator drift, receiver clock slippage and atmospheric propagation errors. These

errors are then added to the local generated P-code to form proper reference signal, which will be used in the fast-time range compression of RC signal. It should be noted that, in this way, the RC range compressed outputs are free of error after compensation. Following up, the slow-time compression is achieved by back projection operation, this is under the help of nominal range history calculated from satellite and receiver position.

The image formation algorithm has been tested with simulated experiment and calibrated with theoretical result from [8]. The simulation parameters are identical to real experiment at Vale village site in Section 3. The real satellite ephemeris is used and receiver position is recorded locally. The image of simulated single target is shown in Figure 6(a), while the theoretical PSF, cross section in North and West direction are shown in (b), (c), (d) respectively.

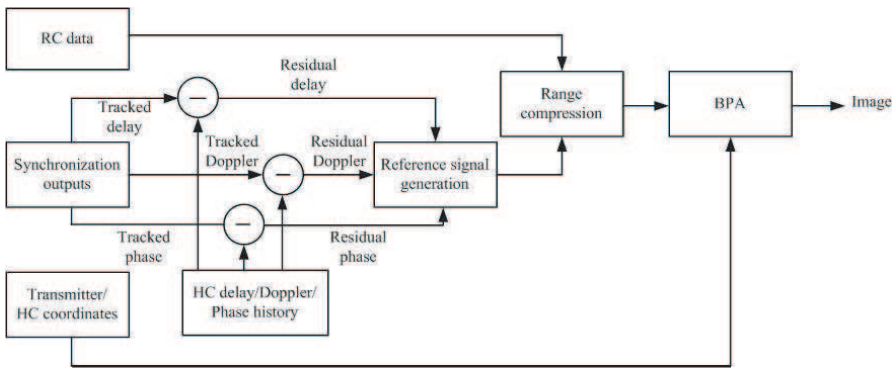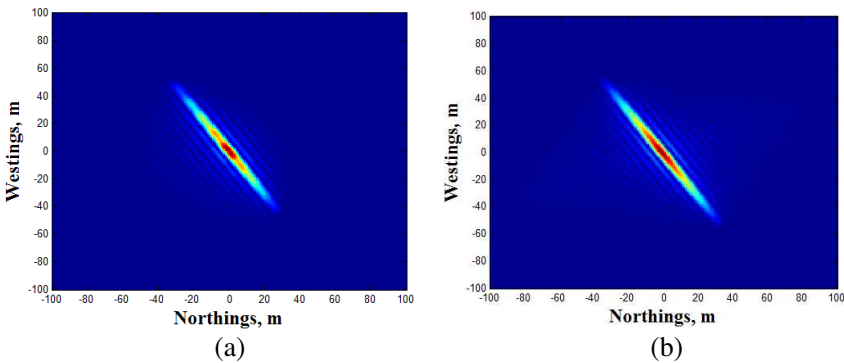The image results in Figures 6(a) and 6(b) are shown using linear

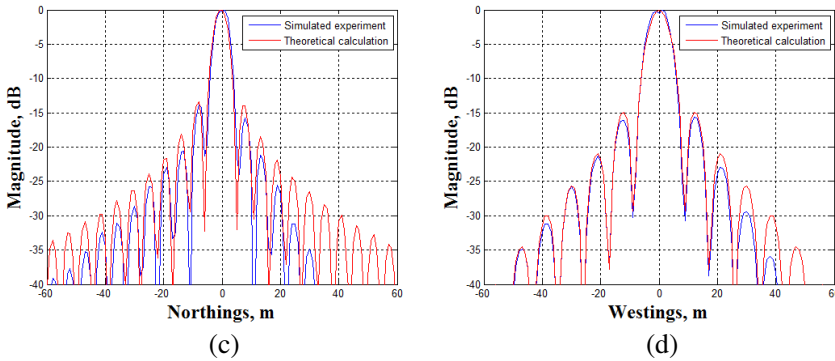**Figure 5.** Flow-chart of signal processing chain for SS-BSAR.

Figure 6. Single target simulation results: (a) simulated PSF, (b) theoretical PSF, (c) cross-section in North direction, (d) cross-section in West direction.

scale, the colour presented are all contrast to the brightest one in the image. It is clear that the simulated PSF and theoretical PSF are much the same in all areas. Furthermore, the cross sections in both directions keep correct shape and align with theoretical benchmark. It should be noted that direction of North and West are defined under local coordinate, which are different from range and cross-range directions. Therefore, the cross section is not strictly sinc-function, but a coupling result between sinc-function and rectangular function resulted from GLONASS pseudo-random ranging signal correlation characteristic.

5. IMAGE ANALYSIS

The experimental program was conducted at Vale village site in the campus of UOB. The target area presented in Figure 7(a) shows the satellite photograph of the whole target area, with a local coordinate (Northings, Westings) for image formation being superimposed on. The two white lines indicate the mainlobe of receiver antenna. The target area features with scattered buildings and plants. There are two major targets, one is Horton grange (Figure 7(c)), which is comprised of three small houses. This building cluster is located near the receiver. The other target is Vale village (Figure 7(b)), which is a newly built, six-layer student accommodation. It is far from the receiver. It should be noted that the irregular shape of roof area of Horton grange make it difficult to predict its reflectivity, however, it is clear that the Vale village building looks like a mirror, which could be served as a prominent single target.
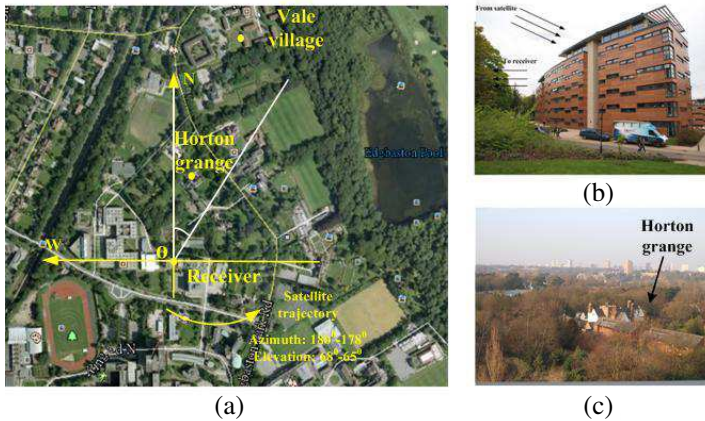
Figure 7. Target area: (a) satellite photograph, superimposed with local coordinate, (b) optical photograph of Vale village, (c) optical photograph of Horton grange building cluster.

Table 1. Experimental acquisition parameters.

Transmitting satellite	GLONASS COSMOS 744
Carrier frequency	1604.8125 MHz
Satellite signal used	P-code (L1)
* Signal bandwidth	5.11 MHz
* Satellite elevation	68°–65°
Satellite azimuth	180°–178°
Integration time	120 s
Bistatic angle	171°
PRF used for signal processing	100 Hz
Expected slow-time Doppler bandwidth	210 Hz

* Satellite elevation angle is measured against horizon observed at receiver location, and azimuth angle is measured relative to North. Both will change during experiment due to satellite moves.

The experimental parameters are listed in Table 1.

The final SS-BSAR experimental image is shown in Figure 8, superimposed with satellite photograph of the same area. This image has been post-processed with windowing and re-sampling to give smooth looking. The image is plotted with the format of two dimensional, from −200 m to 1000 m horizontally, and from 100 m to 1000 m vertically. The colour-scale of the image is in dB scale with the dynamic range from −30 dB to zeros. It should be noted here that
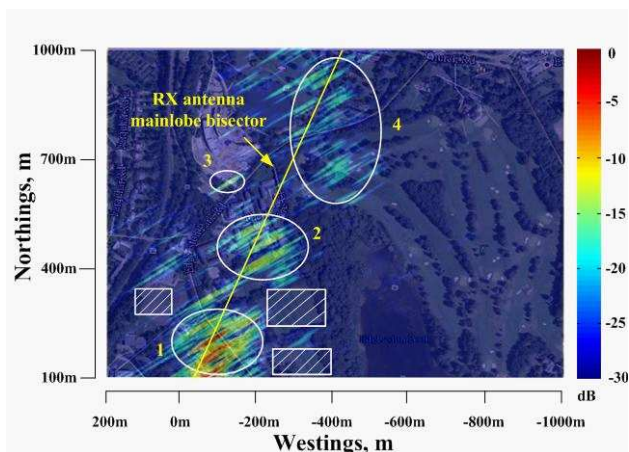
Figure 8. Experimental image overlapped on satellite photograph of the same area.

Table 2. Reflectivity of main targets.

Target	Reflectivity
Horton grange (1)	$-4.91\,\mathrm{dB}$
Tennis court (2)	$-21.21\,\mathrm{dB}$
Vale village (3)	$-17.98\,\mathrm{dB}$
Golf park (4)	$-23.07\,\mathrm{dB}$

the reason why we discard the first 100 m in North direction is that this part of image included PSF of RC antenna, which is formed by direct signal injection to antenna sidelobe and is the highest within the whole image. Removing it will make all the other targets more visible, especially those far way.

Inspection of this final image provides some noticeable information. First, all the prominent reflectivities are one to one match to the real targets. For example, the Horton grange (marked as 1), Vale village (marked as 3). The area of grass demonstrates low signal reflectivity characteristic. Second, the variation of signal intensity coincides with the target-to-receiver distance, close objects perform strong, while far objects weak. The reflectivities of all predominant targets relative to magnitude measured at receiver location are listed in Table 2.

It is more constructive to pay more attention to image details. The image of Horton grange area is shown in Figure 9, which includes two images, the left one is the satellite photograph of this area, the right
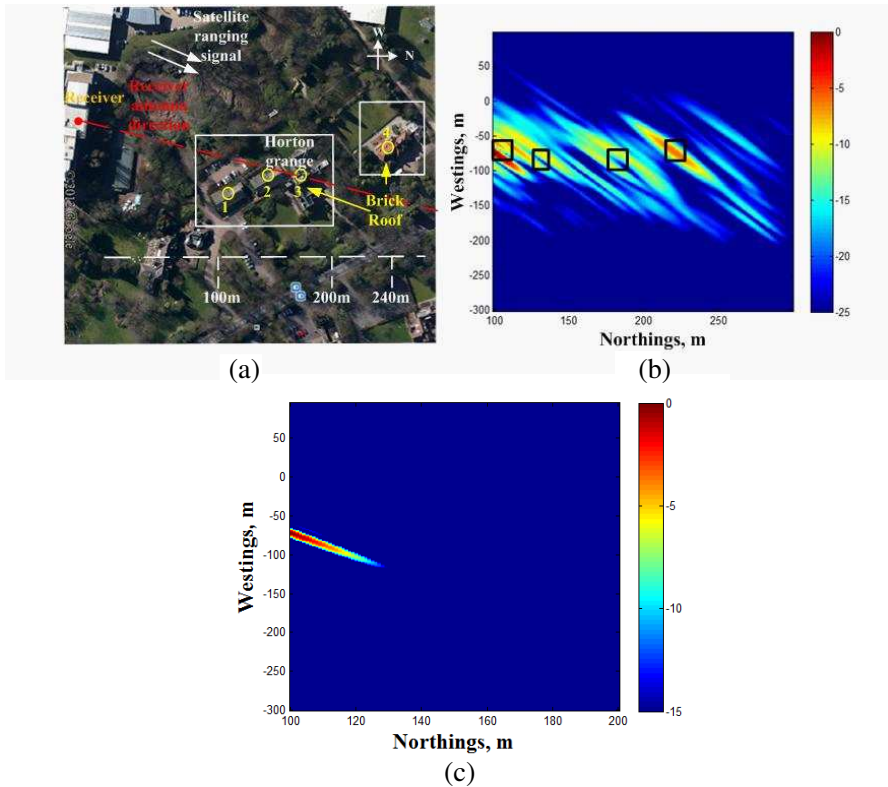
(a)

(b)

(c)

Figure 9. (a) Satellite photograph of target scene '1' in Figure 8, (b) corresponding SS-BSAR image, (c) simulated PSF of building 1.

one is the SAR image. As mentioned before, the irregular roof shape of Horton grange make it difficult to get one to one match with SAR image precisely, and seems there are some extra targets between each buildings. However, a coarse correspondence could still be achieved, the four yellow circles in Figure 9(a) coincide four black squares in Figure 9(b).

Owing to the page limit, we omit the dB plot of cross section, but go directly to the comparison between experimental and theoretical result, which is performed in linear scale. Due to that the four buildings are in a line (not strictly), the cross section in North direction implies them in some extent. Also, from simulation parameters and bistatic geometry, the theoretical PSF could be obtained by point target simulation (Figure 9(c)). Figure 10(a) and (b) show the experimental and simulated cross-sections of building 1 along two North and West

Table 3. Half power width of experimental and theoretical results.

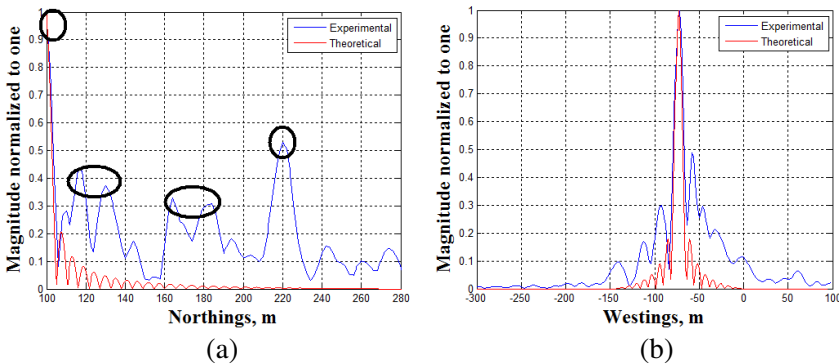|	North direction	West direction
Theoretical width	4.1 m	7.6 m
Experimental width	4.2 m	7.8 m

Figure 10. Comparison between experimental cross section and theoretical cross section: (a) in North direction, (b) in West direction.

directions. The experimental and theoretical width of building 1 in North and West directions are listed in Table 3. The inspection Figure 10 and Table 3 shows that there is a high level of similarity between theoretical and experimental result for a particular target.

Next we check the image performance at Vale village shown in Figure 11(b). The close-in image at Vale village is shown in Figure 11. The left graph is the experimental PSF and the right one is the theoretical counterpart. The experimental result has the same orientation and shape with the theoretical one, except it is a little bit fat. The reason for this may be caused by the inadequate residual phase removal in image formation stage. Moreover, Comparing Figure 6(a) with these two figures, all three come to agreement.

The spatial resolution of SS-BSAR image could be evaluated by checking the response of point-like scatter Vale village in Figure 11(b). The measured 3 dB resolution in North and West directions are 4.1 m and 7.6 m, which is parallel to the theoretical values of 4.2 m and 7.8 m, which are calculated using formula in [8].

It is well worth notifying the returns from area marked with circle 4. This area is covered with trees and grass, and there are no prominent buildings nearby. However, certain amount of signal
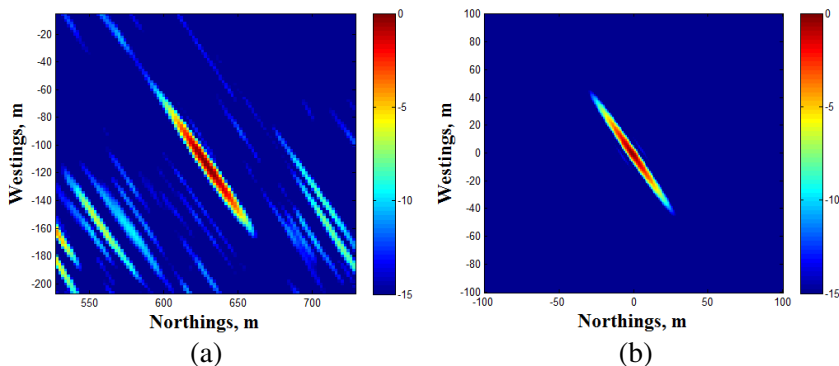
Figure 11. Image of Vale village: (a) experimental image, (b) simulated image.
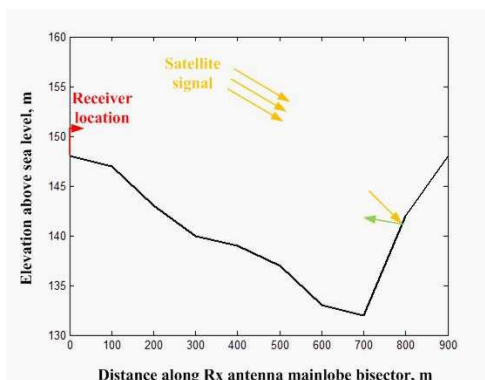

Figure 12. Elevation profile of whole target area.

return is reasonable. The elevation profile along the receiver antenna mainlobe obtained from Google Earth is shown in Figure 12. It could be observed that the sudden height increase of circle 4 area makes this terrain like a mirror. When the satellite signal comes across it, most echoes would be reflected back to the receiver.

Finally, a few remarks will be given to the full-scale image. The dynamic range of the image has been cut down to $-30\,$dB, representing the magnitude of background. The background mainly consists of three components: thermal noise, target response side-lobe and scattering returns from terrain. From power budget calculation in [17], it could be expected that a target with Radar Cross-Section (RCS) of $100\,\mathrm{m}^2$ at $1000\,$m results in magnitude $35\,$dB higher than noise.

Moreover, the property of P-code used for image and long dwelling time indicate compression ratio up to 37 dB in range and 57 dB in azimuth [18]. Therefore, the background is primarily accredited to the terrain scattering.

6. CONCLUSION

This paper reports the experimental imagery results using SS-BSAR with GLONASS and a stationary receiver. Both hardware and signal processing stages leading to final image are described. The core part of the paper is the last section, where we present our latest experimental programs and obtained SS-BSAR image. The comprehensive demonstration of our image proves not only the success but also the stability of such a SAR configuration.

The future work, therefore, owning to the good performance of our system, will be split in two directions. In one way, we will exploit the multi-static imaging to enhance radar vision. In another way, we are subject to the ground feature extraction and classification using this system.

ACKNOWLEDGMENT

REFERENCES

1. Martinsek, D. and R. Goldstein, "Bistatic radar experiment," *EUSAR*, 25–27, 1998.

2. Cherniakov, M., *Bistatic Radar: Emerging Technology*, Wiley, 2008.

3. Wu, J., Z. Li, Y. Huang, Q. H. Liu, and J. Yang, "Processing one-stationary bistatic SAR data using inverse scaled fourier transform," *Progress In Electromagnetics Research*, Vol. 129, 143–159, 2012.

4. Sun, J., S. Mao, G. Wang, and W. Hong, "Polar format algorithm for spotlight bistatic SAR with arbitrary geometry configuration," *Progress In Electromagnetics Research*, Vol. 103, 323–338, 2010.

5. Cherniakov, M., T. Zeng, and E. Plakidis, "Galileo signal-based bistatic system for avalanche prediction," *IGARSS*, Vol. 2, 784–786, 2003.

6. Whitewood, A. P., "Bistatic radar using a spaceborne illuminator," Ph.D. Thesis, 60, University College London, 2006.

7. He, X., M. Chernikaov, and T. Zeng, "Signal detectability in SS-BSAR with GNSS non-cooperative transmitter," *IEE Proceedings on Radar, Sonar and Navigation*, Vol. 152, 124–132, 2005.

8. Zeng, T., M. Cherniakov, and T. Long, "Generalized approach to resolution analysis in BSAR," *IEEE Transactions on Aerospace and Electronic Systems*, Vol. 41, 461–474, 2005.

9. Saini, R., R. Zuo, and M. Cherniakov, "Problem of signal synchronization in space-surface bistatic synthetic aperture radar based on global navigation satellite emissions — Experimental results," *IET Radar, Sonar and Navigation*, Vol. 4, 110–125, 2010.

10. Antoniou, M., R. Saini, and M. Cherniakov, "Result of a space-surface bistatic SAR image formation algorithm," *IEEE Transactions on GRS*, Vol. 45, 3359–3371, 2007.

11. Antoniou, M., M. Cherniakov, and H. Cheng, "Space-surface bistatic SAR image formation algorithms," *IEEE Transactions on GRS*, Vol. 47, 1827–1843, 2009.

12. Antoniou, M., Z. Zeng, F. Liu, and M. Cherniakov, "Experimental demonstration of passive BSAR imaging using navigation satellites and a fixed receiver," *Geoscience and Remote Sensing Letters*, Vol. 99, 1–5, 2011.

13. Sanz-Marcos, J., J. Mallorqui, A. Aguasca, and P. Prats, "First ENVISAT and ERS-2 parasitic bistatic fixed receiver SAR images processed with the subaperture range-Doppler algorithm," *IGARSS*, 1840–1843, 2006.

14. Lopez-Dekker, P., J. Merlano, S. Dugue, J. Sanz-Marcos, et al., "Bistatic SAR interferometry using ENVISAT and a ground based receiver: Experimental results," *IGARSS*, 107–110, 2007.

15. Gong, X. and G. Xu, "Internal time and phase synchronization for distributed micro-satellite SAR," *International Conference on Radar*, 1–4, 2006.

16. End, J. H. G., I. Walterscheid, and A. Brenner, "New aspects of bistatic SAR: Processing and experiments," *IGARSS*, Vol. 3, 1758–1762, 2004.

17. He, X., T. Zeng, and M. Cherniakov, "Signal detectability in DD-BSAR with GNSS non-cooperative transmitter," *IEE Proceedings on Radar, Sonar and Navigation*, Vol. 152, 124–132, 2005.

18. Skolnik, M., *Radar Handbook*, 2nd Edition, McGraw Hill, 1990.